OPTICA

Ultrafast modulation of terahertz waves using on-chip dual-layer near-field coupling

YAXIN ZHANG,[1,2,3,†] KESEN DING,[1,†] HONGXIN ZENG,[1,3,6] WEI KOU,[1] TIANCHI ZHOU,[1] HONGJI ZHOU,[1] SEN GONG,[1,2,3] TING ZHANG,[1] LAN WANG,[1,2,3] SHIXIONG LIANG,[4] FENG LAN,[1,2] YAZHOU DONG,[1] ZHIHONG FENG,[4] YUBIN GONG,[1] ZIQIANG YANG,[1,2] AND DANIEL M. MITTLEMAN[5,7]

[1] *Sichuan Terahertz Communication Technology Engineering Research Center, School of Electronic Science and Engineering, University of Electronic Science and Technology of China, Chengdu, China*
[2] *Yangtze Delta Region Institute (Huzhou), University of Electronic Science and Technology of China, Huzhou, China*
[3] *Zhangjiang Laboratory, 100 Haike Road, Shanghai 201204, China*
[4] *National Key Laboratory of Application Specific Integrated Circuit, Hebei Semiconductor Research Institute, Shijiazhuang, China*
[5] *School of Engineering, Brown University, Providence, Rhode Island 02912, USA*
[6] *e-mail: zenghx@uestc.edu.cn*
[7] *e-mail: daniel_mittleman@brown.edu*

Received 5 July 2022; revised 5 October 2022; accepted 9 October 2022; published 16 November 2022

As a key potential component of future sixth-generation (6G) communication systems, terahertz (THz) technology has received much attention in recent years. However, a lack of effective high-speed direct modulation of THz waves has limited the development of THz communication technology. Currently, most high-speed modulators are based on photonic systems that can modulate electromagnetic waves with high speed using sophisticated optoelectronic conversion techniques. Yet, they usually suffer from low conversion efficiency of light to the THz range, resulting in low output power of the modulated THz waves. Here, we describe a guided-wave modulator for THz signals whose performance nearly matches that of existing in-line fiber-optic modulators. Our results demonstrate a maximum modulation depth greater than 20 dB (99%) and a maximum sinusoidal modulation speed of more than 30 GHz, with an insertion loss around 7 dB. We demonstrate the capabilities of this modulator in a point-to-point communication link with a 25 Gbit/s modulation speed. Our modulator design, based on near-field coupling of a THz transmission line to a single resonant meta-element, represents a powerful improvement for on-chip integrated high-performance THz devices.

https://doi.org/10.1364/OPTICA.469461

1. INTRODUCTION

Developing a device for direct modulation of an electromagnetic signal in the terahertz (THz) range has been a long-standing goal, for the purpose of actively controlling the amplitude [1,2], phase [3,4], and polarization state [5,6] of waves. From the earliest days of THz communications [7], the need for modulators with high speed, high contrast, and low insertion loss has been clear. Many researchers have been involved in this effort, and various approaches have been developed [8–10]. One common scheme is based on the idea of changing the properties of a material component of the device using an external stimulus such as an applied voltage bias [11–20]. Examples include doped semiconductors [11,12], phase transitions in metal oxides [13,14], and graphene [15–20]. This strategy can be combined with resonant structures such as metasurfaces for even more effective device performance. Early work in that direction achieved an amplitude modulation depth of 50% by varying the carrier concentration in a doped GaAs substrate underneath a split-ring resonator (SRR) array [21]. The speed of this device, however, was limited due to the large resistive–capacitive (RC) time constant of the SRR array, which yielded a maximum modulation rate in the kilohertz range. Subsequent developments improved on this performance, for example, by replacing the bulk semiconductor with a double-channel heterostructure, and by replacing the traditional SRR array with a collective dipolar array structure, in order to improve the modulation rate to over 1 GHz [22]. An important step was reported a few years later [23], when the metasurface design was optimized to more effectively control electron transport in the buried two-dimensional electron gas (2DEG), enabling the suppression of parasitic modes and improving the modulation rate to as high as 3 GHz. Yet, this still falls well short of the typical performance speed achieved by electro-optic fiber-based modulators operating at near-IR wavelengths.

One main reason for this gap lies in the fact that nearly all of the work on THz modulators has employed large-area devices suitable for modulating quasi-optic free-space beams. Such large-area devices can exploit phenomena such as collective resonances of many subwavelength elements, to enhance the light–matter coupling [24]. This, however, comes at the cost of an unavoidable contribution to the RC time constant, which sets an upper limit on modulation speed [4,20]. Meanwhile, such planar devices require normal or oblique incidence for the incoming THz wave, so that the devices can work in either transmission [25,26] or reflection [27,28] geometries. This presents significant obstacles to system integration, especially for on-chip systems.

Because of these concerns, researchers are now beginning to turn their attention to the design of waveguide-based modulators, which can be much more compact and compatible with integrated systems. In 2015, two proof-of-principle designs of THz modulators based on waveguides were reported [29], opening the door for the realization of THz waveguide modulators, which combine the relatively low loss of silicon waveguides with the ultra-rapid tunability of the electromagnetic parameters of graphene at THz frequencies. In 2017, a THz modulator was demonstrated by incorporating a graphene sheet on the surface of a passive silicon dielectric waveguide [30]. The experimental results show that the modulation depth can be increased to over 10 dB. This measurement revealed a cutoff frequency of about 2 kHz. This low cutoff frequency is caused by the large RC time constant of the device, which is due to the high-resistivity substrate in combination with the large area of the device. With the goal of reducing RC time, one notable recent result was based on the interaction of THz waves confined within a slot waveguide with a nearby 2DEG [31]. An applied bias modulates the carrier concentration in the 2DEG, thereby varying the loss of the THz guided mode. This work achieved an impressive modulation speed of up to 14 GHz. However, it is difficult to scale these results further, as increasing the interaction length (to increase the coupling of the guided mode to the 2DEG) also increases the switching capacitance. Similar ideas for on-chip integration have recently been executed to enable extremely sensitive THz detection, near the quantum limit [32]. Other recent efforts to enable modulation of guided THz waves relied on optical switching [33], and are therefore less compatible with compact integration.

Here, we describe a new approach to integrated THz photonics that enables modulation rates comparable to the performance of fiber-optic modulators. By combining the controllable transport of charge carriers within a pair of Schottky diodes with an on-chip double-layer individual resonant structure (meta-unit) whose design is inspired by earlier work on metasurface arrays, our device can simultaneously realize a high modulation speed, high modulation depth, and low insertion loss, in an integrated on-chip platform. After chip packaging, the modulator exhibits a monophonic modulation speed of more than 32 GHz, a modulation depth up to 20 dB, and an insertion loss of only 7 dB. To verify its performance, we integrate this component into a point-to-point THz wireless link, demonstrating a data link with up to 25 Gbits/s of throughput.

2. RESULTS

Unlike those used in earlier work on metasurfaces, the proposed structure depicted in Fig. 1(a) is not a collective resonant structure composed of a subwavelength array (see Supplement 1 for the parameters). Instead, it contains an individual resonant element on a double-layer chip. Because this lone active rectangular double-gap SRR is similar to the SRRs used in metasurface arrays, we refer to this element as a meta-unit, and to the device as a meta-chip. One part of the meta-chip is the active meta-unit located on the upper layer of the chip [see exploded view in Fig. 1(b)]. Here, two GaAs Schottky diodes are flipped and embedded across the two gaps of the square resonant meta-unit. This creates a relatively smooth transition between the metal and anode of the diodes, so that it can act as a single continuous metallic resonant unit. The other part of the structure is the on-chip THz transmission line, which is a fin-shaped transmission line on the opposite side of the quartz substrate (thickness 50 μm) [Fig. 1(b)]. A THz wave can be guided along this fin line (along the $+z$ axis in Fig. 1), in an HE hybrid mode whose electric field (in the absence of coupling to the meta-unit) is transverse to the propagation direction and parallel to the gaps in the meta-unit. One side of the meta-unit is grounded to the metallic boundary, while the other side is connected to the external low-pass filter (LPF) line, which we can load with a high-speed digital baseband signal. This external baseband voltage signal affects the electron transport characteristics of the two GaAs Schottky diodes, producing a tunable interaction between the THz wave and the meta-unit.

Figure 1(c) shows the details of the connection between the anode and cathode metals of the GaAs Schottky diodes and the metallic parts of the meta-unit (See Supplement 1 for the parameters). Figure 1(d) shows an optical microscope photo of the meta-chip THz modulator with the two GaAs Schottky diodes. Under the excitation of the external baseband signal, the GaAs Schottky diodes become electron transport channels where the electrons flow between the two disconnected metal rods. This changes the near-field coupling of the guided mode to the proximal meta-unit, and creates a resonant interaction whose frequency is dictated by the geometry of the meta-unit.

Figure 2 summarizes the results of numerical simulations of the device's performance. When there is no baseband voltage applied, the two Schottky diodes are both in the off state, effectively blocking current flow and acting as capacitive gaps across the two arms of the meta-unit. A THz guided wave therefore causes transient charging (current flow) in the same direction across these two diodes, as shown in Fig. 2(a). In this case, there is no resonant interaction between the guided wave and the meta-unit, and the THz wave is coupled to the meta-unit only in the vertical direction (the x axis), as illustrated in Fig. 2(b). The signal can transmit through the fin line with little attenuation, and with little dependence on the geometrical parameters [Fig. 2(c)]. On the other hand, when a baseband voltage signal is applied to the diodes, it lowers the Schottky barrier in the two gaps, so that the Schottky diodes become transport channels for the charge. Thus, electrons can flow across the GaAs Schottky diodes throughout the meta-unit, as shown in Fig. 2(d), producing currents in opposite directions in the two arms of the meta-unit. These oppositely directed currents induce an electromagnetic coupling in the longitudinal direction (the z axis), which acts in addition to the previously mentioned vertical coupling to reconfigure the local electromagnetic mode [Fig. 2(e)]. This three-dimensional coupling manifests a strong resonant interaction for a given frequency, which depends sensitively on the geometrical parameters [Fig. 2(f)].

Using these simulations as a guide, we can adjust the geometry in order to optimize the modulation depth of the device at a chosen operating frequency. The three-dimensional electric field distribution depends on the coupling between the two diodes (longitudinal coupling), which is determined by the longitudinal coupling distance (L) between the two diodes, and on the coupling between the

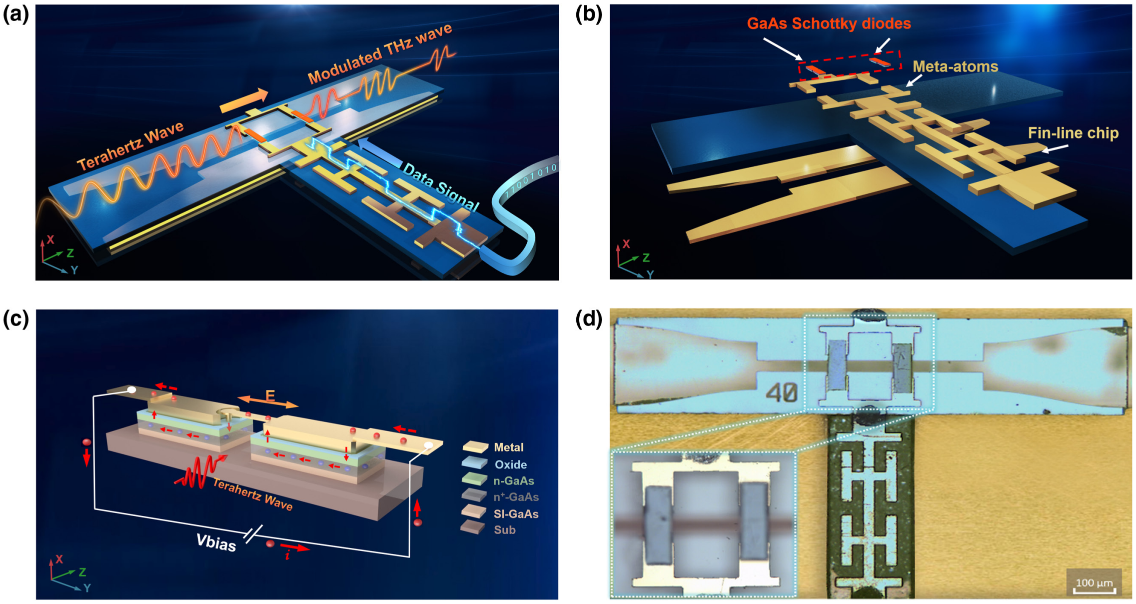

Fig. 1. Overview of the meta-chip. (a) Schematic of the terahertz meta-chip. The baseband signal is fed in by the low-pass filter (LPF) line and interacts with the terahertz wave transmitting on the fin line at the meta-unit. Then the modulated signal emerges at the output of the fin line. (b) The structure of the meta-chip, exploded view. Two GaAs Schottky diodes are flipped on the gaps of the meta-unit. The meta-unit and the fin line are located on the upper and lower layers of the quartz substrate, respectively. (c) The structure of the GaAs Schottky diode and electron transport in the diode under the excitation of a terahertz wave and external bias voltage. (d) Top-down optical microscope image of the meta-chip.

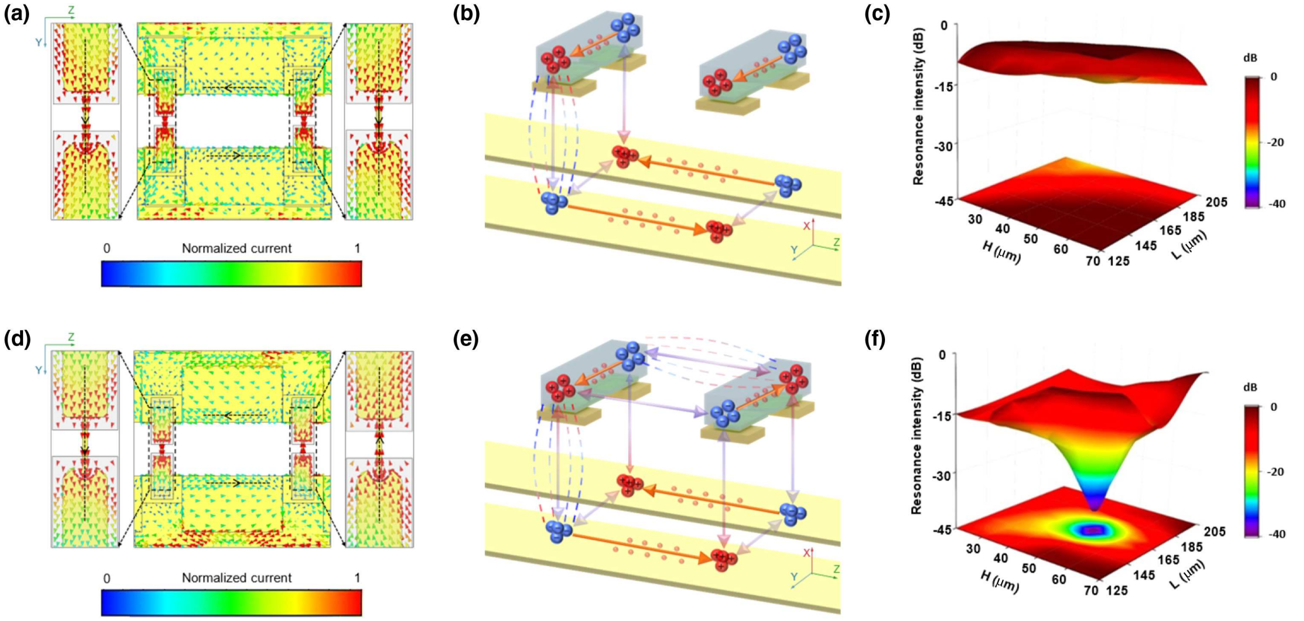

Fig. 2. Electronic properties of the meta-chip. (a), (d) Schematic diagram of three-dimensional coupling mechanism in (a) channel-off state and (d) channel-on state; (b), (e) simulated surface current of the meta-chip at 0.34 THz in (b) channel-off state and (e) channel-on state; (c), (f) simulated resonant intensity in the parameter space covered by H (the thickness of the quartz substrate) and L (the distance between the two diodes) in (c) channel-off state and (f) channel-on state.

fin line and the diodes (transverse coupling), which is determined by the transverse coupling distance (H). Here, we use the terms "longitudinal" and "transverse" with reference to the THz wave's propagation direction. Figure 3 shows additional simulations, which explore the impact of varying the two coupling parameters on the transmission characteristics of the device, at a frequency of 340 GHz. The vertically (z)-directed electric field between the diodes increases with a decreasing longitudinal coupling distance, enhancing the coupling between the two arms of the meta-unit, as shown in Fig. 3(c). At the same time, the resonance intensity also increases when L decreases from 205 to 165 μm [Fig. 3(a)]. This increases up to a point, after which we find overcoupling, which reduces the resonance intensity. Meanwhile, a similar behavior is observed for the transverse coupling distance H. Again, we observe an optimal substrate thickness that produces the largest resonant interaction [Fig. 3(d)] and the highest switching ratio

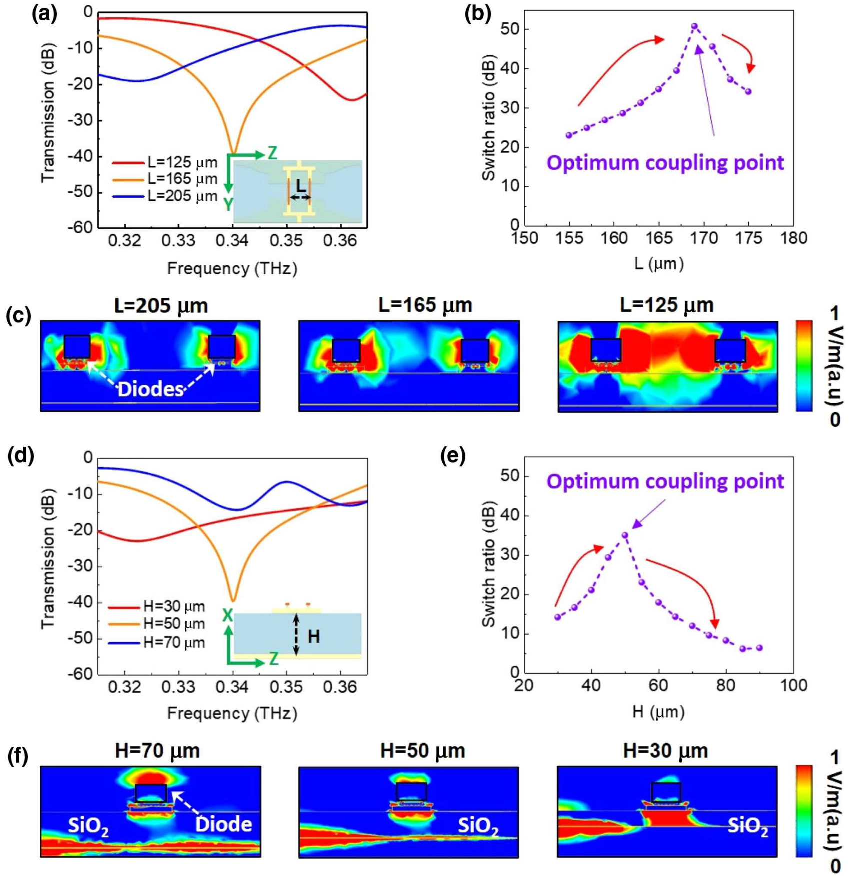

Fig. 3. Three-dimensional electric field coupling of the meta-chip. (a), (d) Transmission characteristic curves for (a) different longitudinal coupling distances (L) and (d) different transverse coupling distances (H); (b), (e) switching ratio values for (b) different longitudinal coupling distances and (e) different transverse coupling distances; (c) simulated z-direction electric field distributions in the channel-on state with different longitudinal coupling distances; (f) simulated x-direction electric field distributions in the channel-on state with different transverse coupling distances.

[Fig. 3(e)]. This corresponds to the largest value for the transverse (x-directed) electric field in the substrate, between the fin line and the meta-unit. As a comparison, the three-dimensional electric field coupling analysis of a meta-chip with a single diode also demonstrates an enhanced effect of the longitudinal near-field coupling between the two diodes on the modulation (presented in Supplement 1).

Based on the simulation results, we fabricate a modulator according to the optimal geometrical parameters, for a target operation frequency of 340 GHz. We then test the modulation depth and the modulation speed of the processed chip. The results are shown in Fig. 4. Figure 4(a) shows the transmission coefficient of the meta-chip as a function of the frequency of the THz wave, under different applied voltages. Without a voltage signal, around 0.34 THz (0.335–0.345 THz), the simulated transmission coefficient (dashed curve) is from −3 to −6.5 dB. When a 1 V signal is loaded, the simulated transmission coefficient decreases to below −20 dB. Consequently, the modulation depth exceeds 17 dB in this frequency range. The experimental results for the modulation depth (solid curves) have slight differences from these simulations (See Supplement 1 for the tolerance analysis). The resonant frequency shifts to 0.347 THz, demonstrating a maximum modulation depth of the packaged meta-chip modulator of up to 20 dB with only 7 dB insertion loss. In a higher frequency band of 0.338–0.352 THz, above the original design frequency, the modulation depth still exceeds 10 dB.

Next, we carry out a modulation speed experiment using a sinusoidal voltage signal. An ultrafast THz detector (0.26–0.4 THz) is used to detect the sinusoidal modulation envelope; the transmitter is a 0.34 THz multichain continuous wave source. As shown in Fig. 4(c), we find a modulation speed as high as 32 GHz, higher than that of any other THz modulator yet reported. These measurements are limited by our experimental capabilities; the cutoff frequency of the SMA connector applied to the packaged module is around 25–27 GHz, so the observed roll-off is likely limited by the packaging and not by the intrinsic speed of the meta-chip. This can be seen in Fig. 4(b), which illustrates the output voltage dependence of the modulation speed. Although there are some fluctuations, which may be caused by impedance mismatch at the signal input port and the limitation of the SMA connector, the voltage amplitude of received signal is relatively flat up to about 23 GHz. Therefore, further optimization of the packaging is likely to produce an even higher modulation speed.

In order to further verify the capability of the meta-chip modulator, we design a THz direct-modulation communication system. The schematic diagram and experiment diagram of the eye pattern test system are shown in Figs. 5(a) and 5(b), respectively. A THz carrier wave at 340 GHz is generated by a phase-locked loop and multiplier–amplifier chain. Then the corresponding high-speed data signal is loaded on the THz carrier wave using the meta-chip modulator and then radiated into free space by a dielectric lens

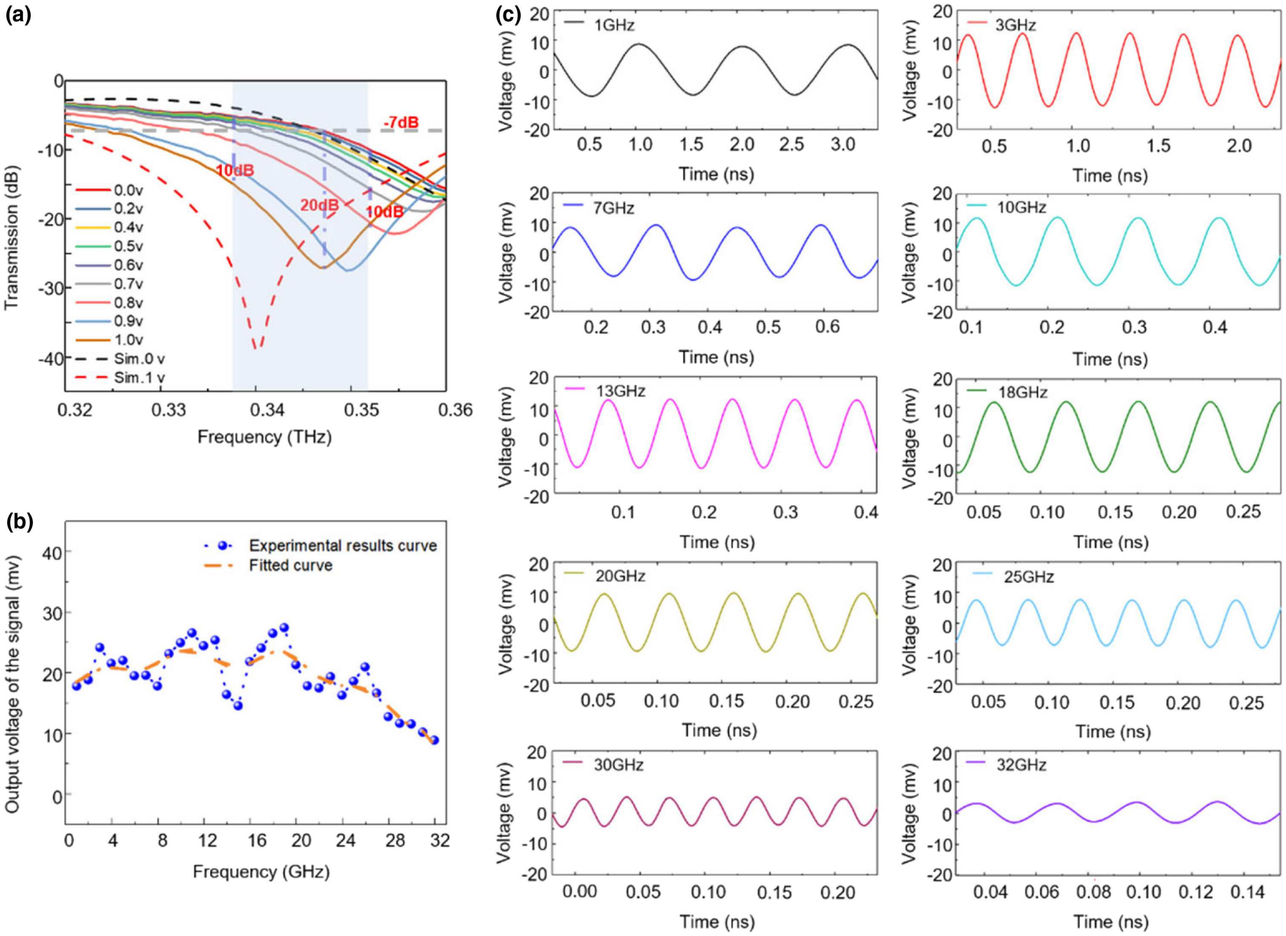

Fig. 4. Sinusoidal signal test of the meta-chip. (a) Transmission characteristic curves for different applied voltages, (b) voltage amplitude of the received modulation signal, (c) waveforms of the received modulation signal.

antenna. The receiver is a Schottky diode envelope detector combined with a wideband low-noise signal amplifier. First we test the system using an arbitrary waveform generator (AWG70001A, Tektronix) and a wideband oscilloscope to obtain high-speed eye patterns. The results in Fig. 5(c) show that this communication system can transmit high-rate signals with a relatively low bit error rate. Because the sampling rate of our AWG is 50 GHz, once the data transmission speed reaches 15 Gbits/s, the signal attenuation and distortion are observed in the eye patterns (see Supplement 1 for the impedance matching for input circuits). Even so, this system achieves a 25 Gbit/s eye pattern transmission with a 10^{-6} error rate over a range of 6 m. Next, using real-time direct on–off keying (OOK) modulation, we construct a THz communication system based on the meta-chip modulator. We note that OOK modulation is a key aspect of existing IEEE 802.15.3d standards for short-range, high-bit-rate communications in the THz bands [34]. Since the modulator supports a high speed and modulation depth, an off-the-shelf field-programmable gate array (FPGA) and comparators can be used to construct the baseband circuits, instead of utilizing a wideband AD/DA chip. This significantly reduces the complexity and power consumption of the system. We demonstrate the video transmission capability of the whole system. A PC at the transmitter end encodes and sends the audio and video signals, while a PC at the receiver end restores the baseband signals to audio and video signals, thus realizing real-time high-resolution uncompressed 4K video transmission (see Supplement 1 for the test frame and site diagram).

3. CONCLUSION

In summary, we have described a THz meta-chip modulator that combines the significant electromagnetic resonant characteristics of a single-element meta-unit structure, the high-speed controllability of a GaAs Schottky diode, and the high integration of an on-chip transmission line. We achieved a maximum modulation depth of 20 dB and a monophonic modulation speed of 32 GHz, consistent with numerical simulations of the device performance. This modulator enables a low-complexity THz direct-modulation communication system, which realizes 25 Gbit/s eye patterns and a real-time 4K high-resolution video transmission. Our strategy of exploiting both longitudinal and transverse near-field coupling in this meta-chip modulator opens up a new way to develop high-performance integrated THz chips. It is not only suitable for single-channel high-speed modulation but also can realize higher-order modulation by synthesizing multiple-channel modulation signals in the future.

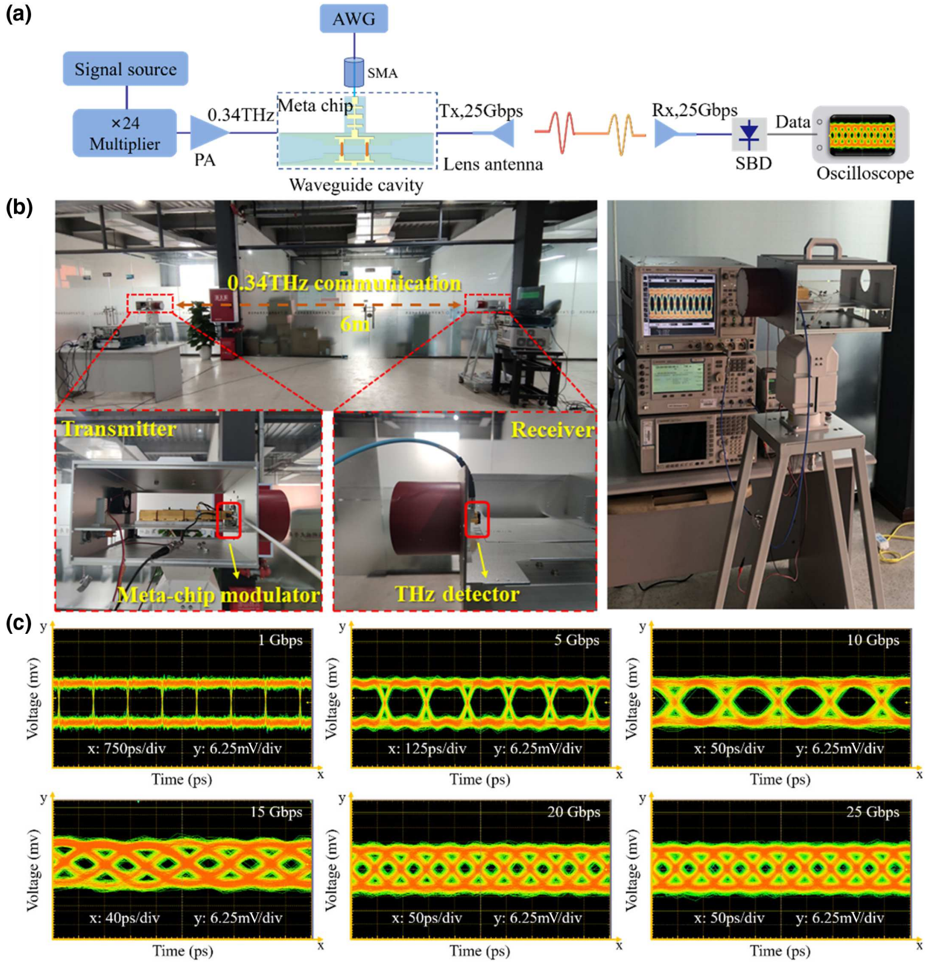

Fig. 5. High-speed data transmission test of the meta-chip. (a) The schematic diagram of the eye pattern test system. The modulation signal output by the AWG is loaded into the meta-chip, and the modulated terahertz wave is detected by the terahertz high-speed detector. PA, power amplifier; SBD, Schottky barrier diode; Tx, transmitter; Rx, receiver. (b) Pictures of the eye pattern test system, (c) eye patterns with 1, 5, 10, 15, 20, and 25 Gbit/s data transmission (Visualization 1). Div, digital input group voltage.

APPENDIX A: METHODS

1. Planar Schottky Diode Fabrication Processes

The preparation of Schottky diodes usually utilizes the method of molecular beam epitaxy [35] to produce wafers with varying doping concentration and thickness. The GaAs substrate and semi-insulating GaAs (SI-GaAs) layer serve as the bottom layer, on which the several doping layers grow; the highly doped buffer layer ($n^+ - GaAs$) is located between the epitaxial layer (n-GaAs) and the SI-GaAs layer, which forms the ohmic contact with the pad. The high doped electron concentration ensures a small ohmic resistance, usually in the order of 10^{18} cm^{-3}; the Schottky contact is composed of the part of the anode metal attached to the n-GaAs layer with a doping concentration of 5×10^{16} cm^{-3} to 5×10^{17} cm^{-3}, which is usually 1–2 orders of magnitude lower than that of the $n^+ - GaAs$ layer [36]. The fabrication of GaAs Schottky diodes can be divided into the following three processes:

(1) Ohmic contact formation. First, use the mask to protect the rest of the wafer after the photoresist is evenly coated on the wafer to ensure that only the photoresist on the wafer region where the ohmic contact is to be formed is exposed to UV light. Next, the photoresist on this region is removed by using the developer solution. After cleaning, the oxide layer and the n-GaAs layer in the ohmic contact area are removed by the etching process, so that the $n^+ - GaAs$ layer is exposed. Then the metal is deposited onto the whole wafer through the thermal evaporating process, with the formation of ohmic contact metals including nickel, gold and germanium alloy, titanium, and gold. Finally, the wafer is placed in the sonic bath to remove the photoresist and the metal on top of it (lift-off), leaving the metal on top of the $n^+ - GaAs$ layer. Thereafter, ohmic contact is formed by annealing.

(2) Schottky contact formation. First, the photoresist is used to protect the position where the Schottky contact will be formed through exposing and developing, and the oxide layer at that position is etched to expose the n-GaAs layer where the Schottky contact will be formed. Then all the photoresist is removed in the sonic bath. After cleaning, the photoresist is developed through exposure again. Finally, the titanium and platinum are deposited on the wafer through e-beam evaporating.

(3) Air bridge and surface channel formation. The gold is then deposited on the wafer to form the air bridge and pad. A diode is basically formed after the excess photoresist and the gold on top of it are cleaned by a stripping process. Finally, the photoresist is used to protect the position of the surface channel that needs to be etched through exposing and developing. The surface channel and

air bridge are formed after etching. After stripping and removing the photoresist, the Schottky diode process is completed by testing and slicing.

2. Device Fabrication

A meta-chip is fabricated on a quartz wafer with a thickness of 50 μm. First, a meta-unit structure with a thickness of 2 μm on the top layer of the quartz substrate is prepared via a photolithography and exposure process. Then, following a similar photolithography and exposure process, a fin line transmission with a 2 μm thickness is deposited onto the bottom layer of the quartz substrate. Next, at the gap of the meta-unit in the top layer, two Schottky diodes are flipped and pasted to the corresponding positions according to the polarity direction by the placement machine. The preparation process of the meta-chip can then be completed. The meta-chip and the fed LPF are accurately placed and fixed in the corresponding slot position of the lower cavity by the assembly machine using a conductive adhesive through the alignment mark. One end of the meta-unit is connected to the externally fed LPF by the conductive adhesive through dot coating. The other end of the meta-unit is connected to the outer wall of the cavity in a similar way to ensure grounding. The fed LPF is connected to one end of the RT-5880 (Rogers Corp., USA) through a bonding wire, while the other end of the Rogers RT-5880 is connected to the external SMA connector. The modulation signal is fed into the GaAs Schottky diode to modulate the THz wave via the SMA.

3. Scattering Parameter Measurement Setup

Vector network analyzers (VNAs) are widely used in ultrahigh-frequency devices to measure the scattering parameters (s) of a single-port or two-port network for performance analysis. A schematic diagram of the sinusoidal signal measurement of the packaged meta-chip is presented (see Supplement 1 for the test frame and site diagram). The VNA (AV3672B, Ceyear, China) covers the frequency range from 10 MHz to 26.5 GHz, and combined with the VNA spread-spectrum module (3643TA, Ceyear, China) can cover 0.26–0.40 THz. VNA and the VNA spread-spectrum module should be calibrated to meet the test requirements before the experiments due to the change in environmental factors over time. The VNA is connected to the VNA spread-spectrum module according to the order of ports. The waveguide ports of two VNA spread-spectrum modules are respectively connected to the packaged cavity, and two connected waveguide ports are fixed with standard screws. The DC source is connected to the SMA connector through the coaxial line. The preset input power of the VNA is -5 to 0 dBm. The scattering parameters (s) of the two-port network are recorded by adjusting the DC source voltage (0–1 V). The DC voltage should be less than 1 V to prevent the Schottky diodes from being damaged.

4. Sinusoidal Signal Measurement Setup

The core dynamic device of the meta-chip is the Schottky diode, whose response to the switching rate of the OOK signal and the attenuation of the signal at high frequencies determines the service transmission capability of the meta-chip. The schematic diagram of the sinusoidal signal test, including the transmitter and receiver is presented (see Supplement 1 for the test frame and site diagram). For the transmitter, a local oscillator (LO) signal with a frequency of 14.167 GHz and a power of 6 dBm is output from the LO source and then fed into the 24 multipliers and amplifier link to generate a 0.34 THz signal, and then the output 0.34 THz signal is fed into the waveguide port of the meta-chip package cavity as a THz carrier. The 24 multipliers and amplifier link is composed of six key components: six multipliers, the power amplifier module, the power divider, two doublers, the power synthesizer, and two doublers. The 4 dBm sinusoidal modulation signal ($V_{pp} = 1$ V) is output from the signal source (0–40 GHz) and then fed into the bias tee (BTN-0050, Marki; $F_{max} = 50$ GHz) together with the DC bias voltage (0.5 V). The output sinusoidal modulation signal (0–1 V) from the bias tee is fed into the SMA connector through the coaxial cable and then loaded into the meta-chip. For the receiver, the modulated signal passes through the attenuator and then is fed into the THz high-speed detector (WR2.8ZBD-F, Virginia Diodes Inc.; $F_{max} = 40$ GHz) to detect its envelope. The THz high-speed detector connects to a high-speed oscilloscope (DPO73304SX, Tektronix) via a coaxial cable whose maximum adoption rate is 100 Gsamples/s ($F_{max} = 33$ GHz).

5. Terahertz Directly Modulated Communication System

The THz wireless communication technology is based on the direct modulation mode [37,38], whose THz source and modulator can be independent to provide a flexible match scheme, which is conducive to reducing the system insertion loss and improving the power capacity of the system. The THz directly modulated communication system (shown in Supplement 1) based on the meta-chip modulator described here is set up to verify the 6 Gbit/s video transmission capability, including the transmitter and receiver. For the transmitter, an LO signal with a frequency of 14.167 GHz and a power of 6 dBm is output from the LO source and then fed into the 24 multipliers and amplifier link to generate a 0.34 THz signal, and then the output 0.34 THz signal is fed into the waveguide port of the meta-chip package cavity as a THz carrier. The 4K video signal provided by a PC is fed into the FPGA (Kintex KCU105, Xilinx) in the form of data packets through the network and then experiences the data process. The spread-spectrum 4K video signal is output from the transmitter port of the FPGA (V_{pp} : 0.4 V) through the coaxial line, and then fed into the bias connector ($F_{max} = 50$ GHz) together with the DC bias (0.6 V). The output video signal (0.4–0.8 V) through the bias connector is connected to the SMA connector by the coaxial line to load into the meta-chip. Then the modulated signal radiates into the free space through the transmitting lens antenna (gain: 48 dBi). For the receiver, the modulated signal is received by a lens antenna 20 m away from the transmitter and then fed into the THz high-speed detector ($F_{max} = 40$ GHz) to detect its envelope. The detected video signal is amplified by a low-noise amplifier (gain: 40 dBi, $F_{max} = 12$ GHz, NF: 3) and then attenuated (15–20 dB). Then, it is fed into the receiver port ($V_{pp} : 0.1 - 0.4$ V) and processed by the FPGA. The decoded 4K video is fed into the PC through the network cable for playback.

Funding. Fundamental Research Funds for the Central Universities (ZYGX2020ZB011); China Postdoctoral Science Foundation (2020M683285); Sichuan Province Science and Technology Support Program (2020JDRC0028); National Natural Science Foundation of China (61771327, 61871419, 6190109, 61921002, 61931006, 62101111, U20A20212); National Key Research and Development Program of China (2018YFB1801503, 2021YFB1401000); National Science Foundation (1923782, 1954780).

Disclosures. The authors declare no conflicts of interest.

Data availability. Data underlying the results presented in this paper are not publicly available at this time but may be obtained from the authors upon reasonable request.

Supplemental document. See Supplement 1 for supporting content.

[†] These authors contributed equally to this paper.

REFERENCES

1. K. S. Reichel, N. Lozada-Smith, I. D. Joshipura, J. Ma, R. Shrestha, R. Mendis, M. D. Dickey, and D. M. Mittleman, "Electrically reconfigurable terahertz signal processing devices using liquid metal components," Nat. Commun. **9**, 4202 (2018).
2. G. Liang, X. Hu, X. Yu, Y. Shen, L. H. Li, A. G. Davies, E. H. Linfield, H. K. Liang, Y. Zhang, S. F. Yu, and Q. J. Wang, "Integrated terahertz graphene modulator with 100% modulation depth," ACS Photon. **2**, 1559–1566 (2015).
3. Z. Chen, X. Chen, L. Tao, K. Chen, M. Long, X. Liu, K. Yan, R. I. Stantchev, E. Pickwell-MacPherson, and J.-B. Xu, "Graphene controlled Brewster angle device for ultra broadband terahertz modulation," Nat. Commun. **9**, 4909 (2018).
4. H.-T. Chen, W. J. Padilla, M. J. Cich, A. K. Azad, R. D. Averitt, and A. J. Taylor, "A metamaterial solid-state terahertz phase modulator," Nat. Photonics **3**, 148–151 (2009).
5. M. Jia, Z. Wang, H. Li, X. Wang, W. Luo, S. Sun, Y. Zhang, Q. He, and L. Zhou, "Efficient manipulations of circularly polarized terahertz waves with transmissive metasurfaces," Light Sci. Appl. **8**, 16 (2019).
6. S. Liu, T. J. Cui, Q. Xu, D. Bao, L. Du, X. Wan, W. X. Tang, C. Ouyang, X. Y. Zhou, H. Yuan, H. F. Ma, W. X. Jiang, J. Han, W. Zhang, and Q. Cheng, "Anisotropic coding metamaterials and their powerful manipulation of differently polarized terahertz waves," Light Sci. Appl. **5**, e16076 (2016).
7. T. Kleine-Ostmann, K. Pierz, G. Hein, P. Dawson, and M. Koch, "Audio signal transmission over THz communication channel using semiconductor modulator," Electron. Lett. **40**, 124–126 (2004).
8. Z. T. Ma, Z. X. Geng, Z. Y. Fan, J. Liu, and H. D. Chen, "Modulators for terahertz communication: the current state of the art," Research **2019**, 6482975 (2019).
9. L. Wang, Y. Zhang, X. Guo, T. Chen, H. Liang, X. Hao, X. Hou, W. Kou, Y. Zhao, T. Zhou, S. Liang, and Z. Yang, "A review of THz modulators with dynamic tunable metasurfaces," Nanomaterials **9**, 965 (2019).
10. R. Degl'Innocenti, S. J. Kindness, H. E. Beere, and D. A. Ritchie, "All-integrated terahertz modulators," Nanophotonics **7**, 127–144 (2018).
11. N. Karl, K. Reichel, H.-T. Chen, A. J. Taylor, I. Brener, A. Benz, J. L. Reno, R. Mendis, and D. M. Mittleman, "An electrically driven terahertz metamaterial diffractive modulator with more than 20 dB of dynamic range," Appl. Phys. Lett. **104**, 091115 (2014).
12. L. Cong, Y. K. Srivastava, H. Zhang, X. Zhang, J. Han, and R. Singh, "All-optical active THz metasurfaces for ultrafast polarization switching and dynamic beam splitting," Light Sci. Appl. **7**, 28 (2018).
13. M. Seo, J. Kyoung, H. Park, S. Koo, H. Kim, H. Bernien, B. J. Kim, J. H. Choe, Y. H. Ahn, H.-T. Kim, N. Park, Q.-H. Park, K. Ahn, and D. Kim, "Active terahertz nanoantennas based on VO_2 phase transition," Nano Lett. **10**, 2064–2068 (2010).
14. L. Liu, L. Kang, T. S. Mayer, and D. H. Werner, "Hybrid metamaterials for electrically triggered multifunctional control," Nat. Commun. **7**, 13236 (2016).
15. Q. Li, Z. Tian, X. Zhang, R. Singh, L. Du, J. Gu, J. Han, and W. Zhang, "Active graphene–silicon hybrid diode for terahertz waves," Nat. Commun. **6**, 7082 (2015).
16. P. Q. Liu, I. J. Luxmoore, S. A. Mikhailov, N. A. Savostianova, F. Valmorra, J. Faist, and G. R. Nash, "Highly tunable hybrid metamaterials employing split-ring resonators strongly coupled to graphene surface plasmons," Nat. Commun. **6**, 8969 (2015).
17. Z. Sun, A. Martinez, and F. Wang, "Optical modulators with 2D layered materials," Nat. Photonics **10**, 227–238 (2016).
18. S. H. Lee, M. Choi, T.-T. Kim, S. Lee, M. Liu, X. Yin, H. K. Choi, S. S. Lee, C.-G. Choi, S.-Y. Choi, X. Zhang, and B. Min, "Switching terahertz waves with gate-controlled active graphene metamaterials," Nat. Mater. **11**, 936–941 (2012).
19. B. Sensale-Rodriguez, R. Yan, M. M. Kelly, T. Fang, K. Tahy, W. S. Hwang, D. Jena, L. Liu, and H. G. Xing, "Broadband graphene terahertz modulators enabled by intraband transitions," Nat. Commun. **3**, 780 (2012).
20. W. Gao, J. Shu, K. Reichel, D. V. Nickel, X. He, G. Shi, R. Vajtai, P. M. Ajayan, J. Kono, D. M. Mittleman, and Q. Xu, "High-contrast terahertz wave modulation by gated graphene enhanced by extraordinary transmission through ring apertures," Nano Lett. **14**, 1242–1248 (2014).
21. H.-T. Chen, W. J. Padilla, J. M. O. Zide, A. C. Gossard, A. J. Taylor, and R. D. Averitt, "Active terahertz metamaterial devices," Nature **444**, 597–600 (2006).
22. Y. Zhang, S. Qiao, S. Liang, Z. Wu, Z. Yang, Z. Feng, H. Sun, Y. Zhou, L. Sun, Z. Chen, X. Zou, B. Zhang, J. Hu, S. Li, Q. Chen, L. Li, G. Xu, Y. Zhao, and S. Liu, "Gbps terahertz external modulator based on a composite metamaterial with a double-channel heterostructure," Nano Lett. **15**, 3501–3506 (2015).
23. Y. Zhao, L. Wang, Y. Zhang, S. Qiao, S. Liang, T. Zhou, X. Zhang, X. Guo, Z. Feng, F. Lan, Z. Chen, X. Yang, and Z. Yang, "High-speed efficient terahertz modulation based on tunable collective-individual state conversion within an active 3 nm two-dimensional electron gas metasurface," Nano Lett. **19**, 7588–7597 (2019).
24. C. Jansen, I. A. I. Al-Naib, N. Born, and M. Koch, "Terahertz metasurfaces with high Q-factors," Appl. Phys. Lett. **98**, 051109 (2011).
25. S. A. Baig, J. L. Boland, D. A. Damry, H. H. Tan, C. Jagadish, H. J. Joyce, and M. B. Johnston, "An ultrafast switchable terahertz polarization modulator based on III–V semiconductor nanowires," Nano Lett. **17**, 2603–2610 (2017).
26. M. Manjappa, P. Pitchappa, N. Singh, N. Wang, N. I. Zheludev, C. Lee, and R. Singh, "Reconfigurable MEMS Fano metasurfaces with multiple-input–output states for logic operations at terahertz frequencies," Nat. Commun. **9**, 4056 (2018).
27. H. Wu, X. X. Gao, L. Zhang, G. D. Bai, Q. Cheng, L. Li, and T. J. Cui, "Harmonic information transitions of spatiotemporal metasurfaces," Light Sci. Appl. **9**, 198 (2020).
28. L. Zhang, X. Q. Chen, S. Liu, Q. Zhang, J. Zhao, J. Y. Dai, G. D. Bai, X. Wan, Q. Cheng, G. Castaldi, V. Galdi, and T. J. Cui, "Space-time-coding digital metasurfaces," Nat. Commun. **9**, 4334 (2018).
29. A. Locatelli, G. E. Town, and C. De Angelis, "Graphene-based terahertz waveguide modulators," IEEE Trans. Terahertz Sci. Technol. **5**, 351–357 (2015).
30. M. Mittendorff, S. Li, and T. E. Murphy, "Graphene-based waveguide-integrated terahertz modulator," ACS Photon. **4**, 316–321 (2017).
31. P. K. Singh and S. Sonkusale, "High speed terahertz modulator on the chip based on tunable terahertz slot waveguide," Sci. Rep. **7**, 40933 (2017).
32. I.-C. Benea-Chelmus, Y. Salamin, F. F. Settembrini, Y. Fedoryshyn, W. Heni, D. L. Elder, L. R. Dalton, J. Leuthold, and J. Faist, "Electro-optic interface for ultrasensitive intracavity electric field measurements at microwave and terahertz frequencies," Optica **7**, 498–505 (2020).
33. T. Sørgård, T. Hawkins, J. Ballato, U. L. Österberg, and U. J. Gibson, "All-optical high-speed modulation of THz transmission through silicon core optical fibers," Opt. Express **29**, 3543–3552 (2021).
34. V. Petrov, T. Kurner, and I. Hosako, "IEEE 802.15.3d: First standardization efforts for sub-terahertz band communications toward 6G," IEEE Commun. Mag. **58**(11), 28–33 (2020).
35. A. Y. Cho and J. R. Arthur, "Molecular beam epitaxy," Prog. Solid State Chem. **10**, 157–191 (1975).
36. Z. Tan, Z. Chen, J. Cao, and H. Liu, "Wireless terahertz light transmission based on digitally-modulated terahertz quantum-cascade laser," Chin. Opt. Lett. **11**, 031403 (2013).
37. N. A. Torkhov, L. I. Babak, and A. A. Kokolov, "On the application of Schottky contacts in the microwave, extremely high frequency, and THz ranges," Semiconductors **53**, 1688–1698 (2019).
38. K. Ishigaki, M. Shiraishi, S. Suzuki, M. Asada, N. Nishiyama, and S. Arai, "Direct intensity modulation and wireless data transmission characteristics of terahertz-oscillating resonant tunnelling diodes," Electron. Lett. **48**, 582–583 (2012).